1

The 2D Semiconductor Library

Zheng Zhang[1,2] *and Yue Zhang*[1,2]

[1]*Academy for Advanced Interdisciplinary Science and Technology, Beijing Advanced Innovation Center for Materials Genome Engineering, University of Science and Technology Beijing, Beijing, China*
[2]*Beijing Key Laboratory for Advanced Energy Materials and Technologies, School of Materials Science and Engineering, University of Science and Technology Beijing, Beijing, China*

1.1 Introduction

Since graphene mechanically stripped out in 2004, two-dimensional-layered materials (2DLMs) have received widespread concern due to the intrinsic changes of the physical and chemical characteristics caused by quantum confinement effect, which pertains to the nanoscale thickness [1, 2]. Since the carrier transport will be strongly restricted to the two-dimensional plane, the electronic and optoelectronic characteristics of the 2DLMs will change significantly [3, 4]. The 2D material family covers various components including most of the elements in the periodic table [5]. These 2D nanosheets usually have a well-defined crystal structure without surface dangling bonds, which has traditionally plagued most semiconductor nanostructures, and therefore exhibits superior electronic properties that are not easily available in other semiconductor nanostructures. This results in a wealth of electronic properties, as well as direct and indirect bandgaps with visible light ranges from ultraviolet to infrared [6–8]. What is more, due to the excellent adaptability of 2D geometry to the existing process techniques in the semiconductor industry, 2DLMs are able to be integrated with conventional semiconducting materials such as silicon and are able to be transferred on diverse supporting substrates. As a result, it is of great potential for them in future applications such as nanoelectronics, optoelectronics, and new ultrathin flexible devices [6–18]. Two-dimensional atomic crystal integrated circuit has been demonstrated, including memory, logic gates, amplifiers, oscillators, mixers, switches, and modulators. Two-dimensional materials of only one or a few atoms thick hold the potential to make future optoelectronics and electronic devices. The functional integrated circuits (IC) of 2DLMs helps solve the technical and fundamental problems of the electronics industry.

Van der Waals Heterostructures: Fabrications, Properties, and Applications, First Edition.
Edited by Zheng Zhang, Zhuo Kang, Qingliang Liao, and Yue Zhang.

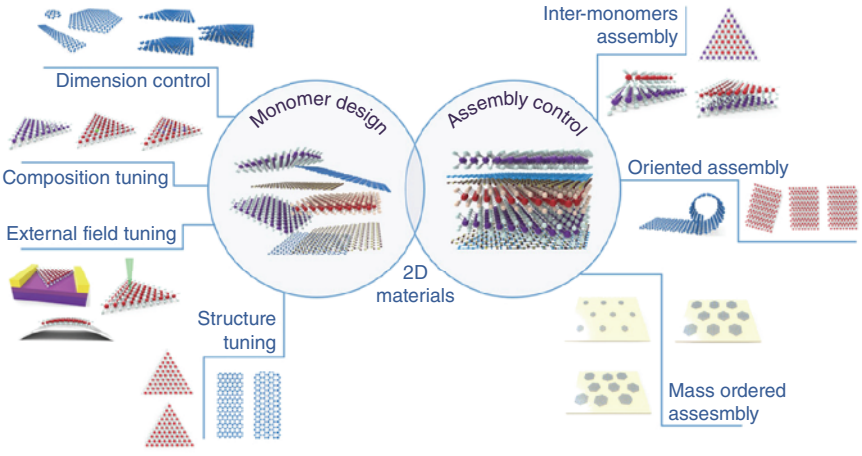

Figure 1.1 Two-dimensional materials for future electronic devices: from cell unit to small integration. *Source:* Reproduced with permission from Ref. [19], © American Chemical Society 2018.

The emerging application of nanoelectronics using two-dimensional materials prerequisites a reliable preparation and controlled stacking of wafer-scale 2DLMs of high quality by taking full advantage of their unique features in the two-dimensional limit (Figure 1.1). The widespread use of 2DLMs is due to their inherent properties and, to a large extent, their adjustability. Because of the novel anisotropy and planar crystal structure of 2DLMs, their properties can be improved greatly by adjusting the composition, size, field, and structure [20]. For instance, the band structure of a two-dimensional material changes significantly as the material thickness decreases from block to single-layer limit. In addition, some two-dimensional materials can be converted from semiconductor to metal through the intercalation. The use of one material in modern technology and applications is difficult to achieve a variety of excellent performance. As a result, 2DLMs can adjust their properties to the desired functionality, opening the way for further widespread use in electronic circuits.

Furthermore, since only one or a few atoms thick, 2DLMs with different heights can be stacked to form various heterostructures without consideration of lattice matching and processing compatibility. Van der Waals (vdW) heterostructures with sharp interfaces and disparate electronic properties offer a novel platform and prosperous applications for investigation of the creation, confining, and transmission of charge, excitons, and photons at two-dimensional limit [18]. The structure of a single two-dimensional material is also worth further study because it helps to further discover the intrinsic properties of the 2DLMs. New applications can be made by extending the structural deformation derived from directional construction to the properties of 2DLMs. In addition, efficient construction techniques are disposable to the production of large-scale nanodevices with desired-ordered structures to address the scaling and integration challenges of microelectronics, photonics, and microelectromechanical systems [21–24].

1.2 Emerging 2DLMs for Future Electronics

The rise of graphene with excellent properties has facilitated the discovery and research of new two-dimensional materials. In addition to graphene, various two-dimensional materials are attracting focus because of their unique properties. The size effect and adjustability of its energy band structure result in some novel properties. In this section, we will look at two aspects of the emerging 2DLMs. In one part, we will give clues based on the structure of two-dimensional materials, and in the other part, we will detail the various 2DLMs that are classified by their elemental composition.

1.2.1 Classification

Initially, 2DLMs represented by graphene were referred to as a layered material that has strong intralayer covalent bonds and weak interlayer vdW coupling. Therefore, the layered material can be obtained by stripping the bulk material. In this case, we call them two-dimensional layered materials (2DLMs).

Lamellar vdW materials, which are separated into single or several layers, are one of the hot research topics. Due to the strong covalent bonds in planes and weak interlayer vdW coupling, they can be separated by mechanical or liquid stripping to form nanosheets [8, 25]. In addition to graphene, which was first discovered, transition metal dichalcogenide (TMDCs) are also typical vdW materials, such as MoS_2, WS_2, and WSe_2. To date, more than 40 types of TMDCs have been discovered [26]. Hexagonal boron nitride (h-BN) [27], silicon carbide [28], VO_2 [29], and telluride antimony [30] are also included within such category.

1.2.2 Elemental 2DMLs

2DMLs such as III-VA group and transition group are of great interest. Because of their unique ultrathin two-dimensional limit, they exhibit superior electronic, photonic, magnetic, and catalytic properties than bulk materials. These materials are of great potential for diverse applications in field effect transistors (FET), optoelectronics, memories, and artificial synapsis [31].

1.2.2.1 IV A Group

Since its discovery in 2004, graphene with the feature of honeycomb structure has been attracting great attention [2]. A range of methods for preparing graphene, such as mechanical stripping, liquid-assisted stripping, and chemical vapor deposition (CVD) methods, have rushed out. It has lots of superior properties, in particular its unprecedented high intrinsic mobility of $200\,000\,cm^2\,V^{-1}\,s^{-1}$ at room temperature [32]. Stampfer et al. discovered that it has the mobility at low temperature of $350\,000\,cm^2\,V^{-1}\,s^{-1}$, as shown in Figure 1.2a, reaching the highest record so far [35]. The grooves are utilized to suspend graphene. The beam of laser is concentrated on graphene, after which the heat flows radially from the graphene center to the peripheral. The dependence of Raman G peak on excitation power is measured, and

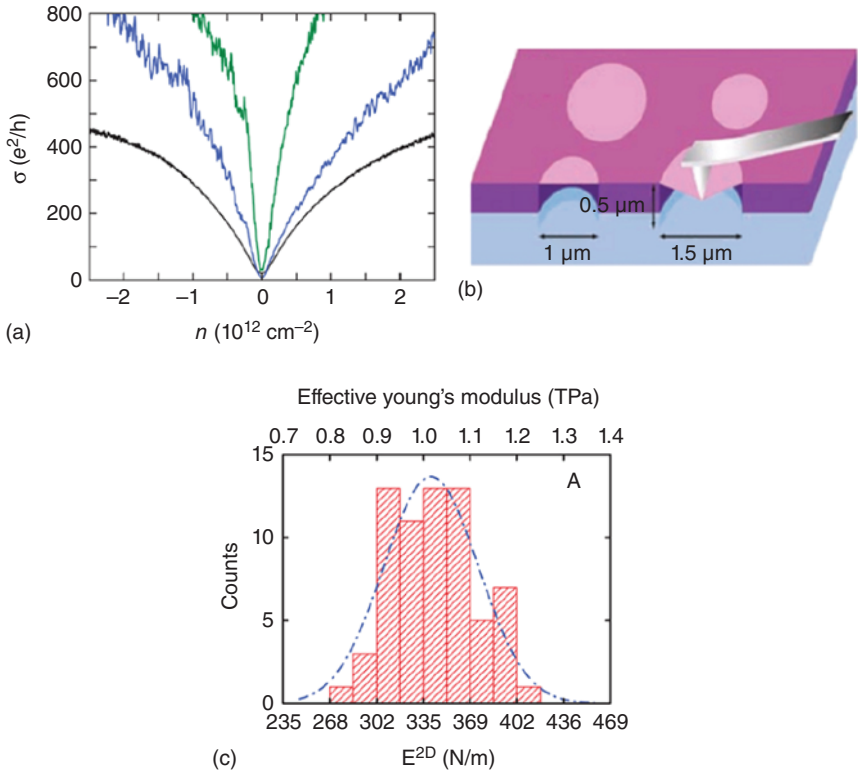

Figure 1.2 Brief introduction of graphene. (a) Relationship between conductance and density of charge carrier. The black and blue plots were obtained at 300 and 1.6 K, respectively. The green one is consistent with carrier mobility $\mu = 350\,000\,cm^2\,V^{-1}\,s^{-1}$ from another sample. *Source:* Reproduced with permission from Ref. [33], © American Chemical Society 2008; (b) schematic of configuration about suspended graphene being indentated. (c) Elastic stiffness statistics histogram of graphene. *Source:* Figure (b) and (c) reproduced with permission from Ref. [34], © Wiley Online Library 2010.

the TC of graphene is approximately $5000\,W\,m^{-1}\,K^{-1}$ [33]. Graphene was suspended, and Young's modulus was characterized by patterning a circular well array having a 1.5 mm diameter and 500 nm depth on a SiO_2/Si substrate (Figure 1.2b). Figure 1.2c shows the elastic stiffness statistical histogram of suspended graphene. Young's modulus obtained by this method is about 1.0 T Pa [36]. Therefore, graphene has shown great prospect in applications of electronics, optoelectronics, energy storage, and conversion.

However, graphene still faces significant challenges because of its zero-bandgap nature, which hinders its eventual application. Another two-dimensional allotrope of carbon breaks the ice. The graphite acetylene and its derivatives composed of sp- and sp^2- hybrid carbon atoms have a certain bandgap in the band structure [37–39]. In graphene-acetylene and its derivatives, the alkyne bond is a structural unit that can be inserted to modify the graphene and retain the symmetry of the hexagon. Figure 1.3a shows the transformation of graphene to α-, β-, and γ-graphene by

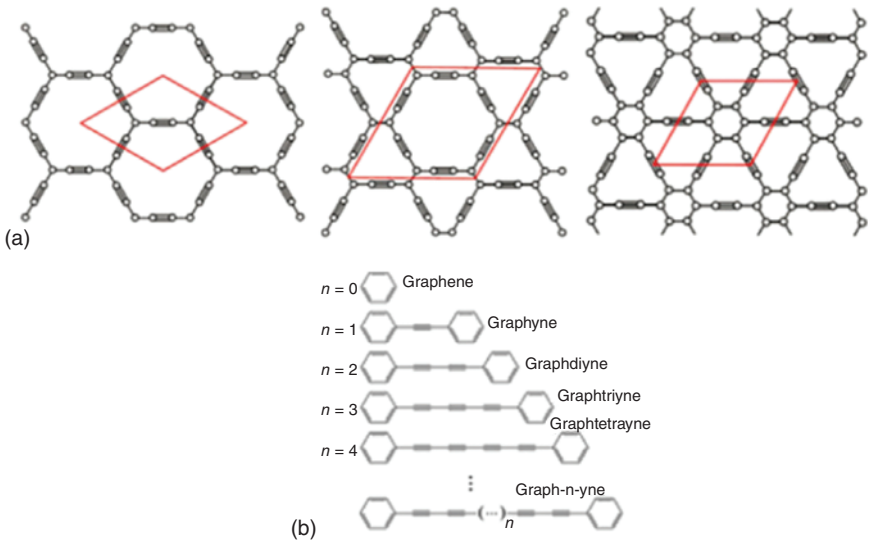

Figure 1.3 Structure and optoelectronic applications of graphite–acetylene group materials. (a) Structure of alpha-, beta-, and gama-graphene. *Source:* Figure (a) reproduced with permission from Ref. [39], © American Chemical Society 2011; (b) expansional diagram of n-alkyne based on chain length. *Source:* Reproduced with permission from Ref. [40]/ © American Chemical Society 2013.

inserting acetylene bonds between two carbon atoms in different ways [38]. The structure shown in Figure 1.3b is formed by graphite diacetylene when two acetylene bonds are inserted [39]. Acetylene chains of different lengths will generate a series of graphitic alkynes, such as graphitic alkynes, graphitic dialkynes, graphitic trialkynes, and graphitic tetrapyne. [41]

As one of the graphyne derivatives, graphdiyne can be grown by cross-coupling with hexaethynylbenzene as precursors [40, 42–45]. In general, graphdiyne can be obtained as nanowalls (NWs) [44, 45], film [42, 43], or coating layers covering TiO_2 [40] by this coupling reaction. In recent years, graphdiyne was successfully prepared on the Au (111) crystal plane using molecular evaporator deposition of precursor molecules in the ultrahigh vacuum ambient of an scanning tunnelling microscopy (STM) [46]. Nishihara et al. successfully prepared multiple layers and few layers of graphite-diacetylene through liquid/liquid or gas/liquid interface reactions [47]. Its properties are predicted successfully by theoretical calculation. Graphyne allotropes feature an intrinsic bandgap (~ 1.2 eV for graphyne and ~ 0.46 eV for graphdiyne), and their direct bandgaps indicate their potential applications in optoelectronic devices [48, 49]. Two-dimensional graphene with Dirac dots and cones still exist, such as α-graphene with a single Dirac cone and 6,6, 12-graphene with two different Dirac cones [49, 50]. The different atomic structure of graphyne alkyne results in the difference of electronic structure [51]. Graphyne group material as a new 2DLM has excellent application prospects in electronic devices and photovoltaic devices [40, 43, 49]. Li et al. constructed a solar cell with

high efficiency electron transport based on graphite-diacetylene doped benzene-C61-methyl butyrate, as shown in Figure 1.3 [52]. Although graphyne family materials have excellent carrier mobility with a proper bandgap, the challenge of synthesizing single crystal with large scale and high quality has severely limited the further application development of graphite-based alkyne. Wherefore, new methods are urgently needed to achieve the preparation of such high-quality materials.

In addition to carbon, other elements of the IVA group can also form 2DLMs, including silene, germanene, and tinene. The atoms in silicene or germanene are connected with each other through sp^3 hybridization, which is more stable than the sp^2 hybridization. Even if they are not able to exist as independent lamellae, they can still be successfully obtained as layered materials. At present, lots of methods have been reported to grow silene. One of the most effective methods of wet chemistry is the stripping of 2DLMs by an exchangeable Ca layer and an interlinked Si6 ring consisting of $CaSi_2$ [53]. Some used HCl solution and Mg to further reduce layer-to-layer interactions [54, 55]. In addition, the most common approach is the vapor deposition on selected substrates, such as Ag (111) [56], Ag (110) [57], Au (110) [58], Ir (111) [59], MoS_2 [60], ZrB_2 [61], and H-$MoSi_2$ [62] in STM. Excellent physical features of silicene, including the quantum spin Hall effect [63, 64], ferromagnetism [65, 66], germanium doping controlled TC [67], and semi-metallic properties [68] have been predicted by theoretical calculations [69].

Germanene can be prepared in a comparable method as silicene, including $CaGe_2$-assisted chemical exfoliation [70] and vapor deposition [71–73]. Germanene features a number of exclusive characteristics, including robust structure [74], semimetallic property [75], high exciton resonance [76, 77], high carrier mobility [78], Dirac characteristics [79, 80], photon properties of ground state [81, 82], negative thermal expansion [83], spin electron transport [84], tunable magnetism [85], many body effects [86], infrared absorption [87, 88], and great thermoelectric properties [89]. The charge carriers of germanium materials, whose electronic structure is similar to graphene and silicon, are massless fermions. Using a vertical electric field can open the bandgap in a single layer of flexed silicon and germanene [90]. In addition, novel properties of the quantum spin hall effect are able to be realized by halogen or hydrogen elements modification [91, 92].

The Sn (111) diatomic layer where two triangular sublattices are stacked to generate a crooked honeycomb lattice that forms the stanene. Based on the substrate Bi_2Te_3 (111), stanene can be prepared by molecular beam epitaxy (MBE) [93]. Excellent properties have been predicted through theoretical calculations [94], such as stress-affected mechanical properties, novel thermal transport diffusion properties [95, 96], unique electronic features [97], phase transition between topological phase to insulating one [98], large magneto-resistive [99], super conductivity [100], and quantum spin Hall effect [101].

1.2.2.2 V group A

Two-dimensional materials composed of V-A group elements include black phosphorus (BP), arsenic, antimony, and bismuth. In 1914, BP was successfully prepared [102, 103], where each atom was covalently connected to three adjacent atoms

to create a folded monolayer honeycomb. [104] From bulk to monolayer, the bandgap of BP increases (0.3 up to 1.5 eV). In addition, it has been proved that the room temperature carrier mobility of BP in several layers of quasi-2D phosphors is up to 1000 $cm^2 V^{-1}s^{-1}$ [105]. Therefore, BP shows significant prospect in applications of electronic and photonic devices [106]. Current methods for producing BP include mechanical stripping [107–109], liquid stripping, [110–113] and CVD [114]. At the same time, the thickness of BP determines its properties, for example photoluminescence (PL) spectroscopy [109, 110]. BP has been demonstrated to show great potential applications in photoelectric fields [107], including photodetectors and solar cells. [115] BP is studied through simulation experiment and theory analysis of many properties, including stacking-sequence-dependent electronic structure [116–118], anisotropic properties [114], transmission characteristics between magneto-optical [119], controlled band structure [120, 121], flexibility [122], thermal properties [123], anisotropic exciton [124], and electrical conductance [125]. Interestingly, blue phase [126, 127] and topological insulator conversion of BP are proved [128].

Structurally, a layer of arsenic atoms with a rhombic structure forms arsenic. Thickness of 14 nm arsenic was successfully grown on InAs substrate via plasma-assisted process [129]. It has been theoretically calculated that arsenic has many exclusive characteristics, covering anisotropic-controlled TC [130] and strain-modulated topological insulator conversion [131].

The most stable V-A group allotropes is antimonene with monolayer antimony. The bandgap is predicted as 2.28 eV. At present, the approaches of preparing antimonene are mainly mechanical stripping [132], liquid exfoliation [133], MBE [134], and CVD [135]. Antimonene is predicted theoretically to feature some novel characteristics, including spin–orbit coupling (SOC) effect [136], geometry-controlled TC [137], defects-controlled electronic properties [138], and UV detection [139]. Indirect to direct bandgap transition would occur through a small stress, further advancing its potential in optoelectronic applications [140, 141].

In 2005, bismuth was first grown on atomically smooth surfaces [142]. After that, bismuth was successfully obtained by wet chemical synthesis [143]. Theoretical calculations show that bismuthene has a lot of nice attributes. At high temperature, bismuth is insensitive to long wavelength vibration and thermal excitation. As the 3D bulk is scaled into individual single-layer sheets, the bismuthene's structure is compressed, resulting in a transformation from a semi-metal to a semiconductor. Nevertheless, such thickness dependence does not affect the topological characteristics of bismuthene [144, 145].

1.2.2.3 III A Group

In Group III A, the last specific elemental 2DM is borophene. Boustani first proposed the quasi-planar boron structures through theoretical calculations [146]. Later, methods for preparing borophene, such as vapor deposition [147, 148] and two-growth-zone CVD, were reported [149]. More simulations show that borophene has lots of special attributes, such as high work function [150], magnetism [151], and extremely high hydrogen storage capacity [152]. In addition, two-dimensional

borophene has potential applications of power generation, electrical transmission, energy storage, and electrocatalysis [153, 154].

1.2.3 Hexagonal Boron Nitride (h-BN)

After the discovery of graphene, atomically thin h-BN has also attracted continuous attention in the field due to excellent performance and potential application prospects. The single-layer h-BN has a crystal structure similar to graphene, so it is often referred to as "white graphene." It consists of alternating covalent B and N atoms in a hexagonal basal plane (space group = $P6_3/mmc$) and is free of dangling bonds between the layers (Figure 1.4a,b). These layers stack together to form the bulk crystal by the vdW force [159]. The bulk h-BN shows lattice constants ($a = 2.504$ Å) and interlayer distances (3.30−3.33 Å) [155].

Having different physical properties from graphene, h-BN is a typical insulator with high relative permittivity and an indirect bandgap of about 6 eV. In addition, h-BN has many other properties including chemical stability, thermal stability, high TC, great mechanical flexibility, atomically flat surface, free of dangling bonds, and charged impurities [156]. This makes h-BN in the field of microelectronics, especially in the vdW electronic field, a broad application prospect. First, h-BN is an appealing substrate dielectric for 2D material-based devices [160]. Compared with traditional substrate dielectric, graphene and other two-dimensional materials using h-BN as dielectric substrate can improve the carrier mobility and realize rapid

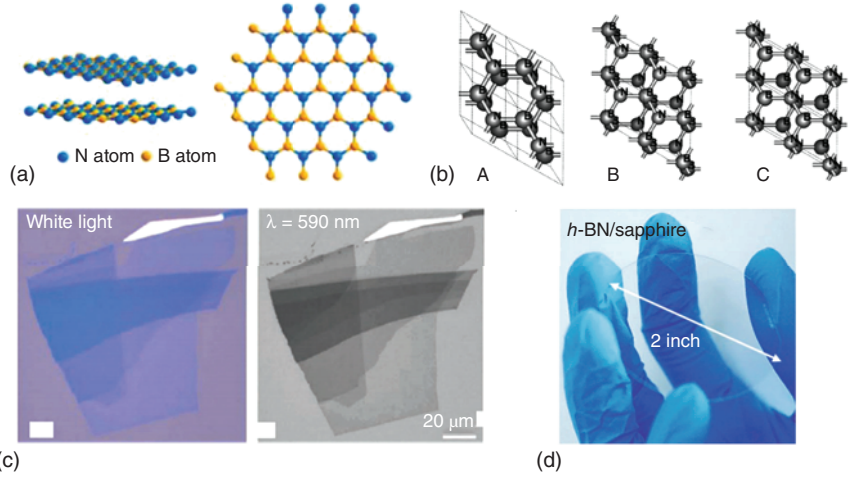

Figure 1.4 (a) Crystal structures of h-BN. *Source:* Reproduced with permission from Ref. [155], © Chemical Reviews 2017; (b) three structures of h-BN all have space group P63/mmc and can be transformed into one another by translational gliding moves of the BN plane. *Source:* Reproduced with permission from Ref. [155], © Physical Review B 2003; (c) exfoliated h-BN nanosheets from h-BN single crystals on the 90 nm SiO_2 substrate. *Source:* Reproduced with permission from Ref. [156], © Nano Micro small 2011; (d) photograph of a wafer-scale SC-hBN film on a SiO_2-Si wafer. *Source:* Reproduced with permission from Ref. [157, 158], © Advanced Materials Interfaces 2018.

heat dissipation at the same time. This can significantly improve the device performance while maintaining the intrinsic performance of the channel material. Second, the high stability and two-dimensional honeycomb structure of h-BN can be applied in device packaging [161]. The dense six-membered ring structure of h-BN can isolate the influence of external atoms on internal devices, protecting the TMDCs channel material from the corrosion of water and oxygen in the air. Furthermore, the tunable tunneling barrier of h-BN has potential applications in tunneling, optoelectronic, and memory devices [162]. Recently, it has been found that h-BN, as a natural hyperbolic and piezoelectric material, exhibits some new optical and electromechanical properties [163]. These unique properties also make it a candidate for practical applications of hyper lenses, near-field imaging, deep ultraviolet emitters and detectors, quantum optoelectronics, and nonlinear and stretchable optical devices [164].

Obtaining large-size and high-quality h-BN film is the primary problem for realizing its application. Up to now, h-BN is usually prepared by mechanical exfoliation and CVD. The mechanical exfoliation can achieve high-quality and few-defect h-BN flakes (Figure 1.4c), but due to the small size and limitation of yield, it is usually used for proof-of-concept of a single prototype device. CVD is considered to be an ideal solution for low-cost, high-reproducibility, and large-scale preparation of h-BN. The current breakthrough in CVD growth of h-BN is the successful preparation of wafer-scale single-crystal film (Figure 1.4d) [157]. Besides, other 2D materials can be epitaxially grown directly onto h-BN by CVD method to form high-quality heterostructures with clean interface and controllable stacking sequence [165].

1.2.4 Transition Metal Dichalcogenides (TMDCs)

Two-dimensional TMDCs are a class of promising materials with attractive properties in the basic research of new physical phenomena and applications in fields ranging from electronics and photonics to sensing and actuation. The generalized formula of TMDCs is MX_2 where M and X are transition metal element and chalcogen element (S, Se, or Te), respectively. MoS_2 monolayers have demonstrated the applications of transistor [11] and PL since 2010. After that, TMDCs are regarded as highly promising candidates for next-generation electronics and photonics [166, 167].

Recently, the vdW integration primarily stimulated 2D device research. The high-quality vdW heterostructures with low production cost and short development processes are reported and applied in the field of physics and electronics [168, 169].

Most TMDCs are dangling bonds free and thus exhibit high mobility. Meanwhile, the selection of suitable substrate, metal contact, and mobility restrain caused by grain boundaries are also crucial for electronic device [170]. For example, mobility of MoS_2 on SiO_2/Si substrate with BN/Si substrate (encapsulated) and scandium contact is 33–151 $cm^2\ V^{-1}\ s^{-1}$ and 700 $cm^2\ V^{-1}\ s^{-1}$ at room temperature, respectively [171, 172].

The structure of TMDCs was first reported in 1923 by Linus Pauling. After that, around 60 TMDCs were found in the late 1960s [173]. The ultrathin MoS_2 layers are obtained by tape exfoliation by Robert Frindt in 1963 [174]. Monolayer MoS_2

suspensions were produced in 1986 [175]. Since 2004, the rapid development of graphene-related research has led to the development of technologies for layered materials, opening a new way for research on TMD, especially for ultrathin films [176].

Here we will introduce the structure and electronic band structure of TMDCs. The typical atomic ratio of TMDCs (MX_2) is one transition metal atom (Ti, V, Ni, Zr, Nb, Pd, Hf, Ta, Ir, Pt, Mo, and W) stuck in two chalcogen atoms (S, Se, and Te), while some other cases are 2 : 3 (M_2X_3) with quintuple layers, or 1 : 1 (MX) [177–179].

Stacking sequence affects the electronic band structure, phonon vibration, optical properties, and other outstanding physical properties of the material [180]. There are two common structural phases of TMDCs that are 2H and 1T. The H and T are the acronyms of hexagonal phase with trigonal prismatic structure and tetrahedral phase with octahedron structure, respectively. The stack sequence of TMDCs is indicated in the numbers of phase name such as "2" H, "1" T, "3" R, and "4" H. For example, 2H-MoS_2 possesses a two-layer AB stacking, and 3R-NbS_2 possesses a repeating three-layer ABC stacking. The H-phase material belongs to hexagonal symmetry, and each metal atom extends six branches out to two tetrahedrons in z and +z directions. The chalcogen-metal-chalcogen arranged along z direction are considered to be monolayer, and the vdW interaction between each layer (chalcogen–chalcogen) is weak, which makes the bulk TMD mechanically easy to peel into a monolayer flake [178]. The T-phase structure TMDCs consists of a trigonal chalcogen layer on the top and a 180-degree rotation structure at the bottom. The stacking configuration of the individual layers in multilayer and bulk samples and possible distortions further describe the structure of TMDCs [181, 182]. These pronounced distortions can lead to the formation of metal–metal bonds, which result in the 1T′ phase in the dimerization of the 1T phase of group VI TMDCs. The charge density wave phase is also associated with the weak lattice distortion that shows rich physics and complex phase diagrams.

Except for WTe_2, the 2H phase and 1T phase common bulk phase TMDCs formed by VI transition metals (Mo or W) and chalcogen (S, Se, or Te) are thermodynamically stable and metastable, respectively. Orthorhombic 1T′ phase WTe_2 is the stable bulk phase that is different from other TMDCs. The cohesive energy difference between 1T′ phase and 2H phase $MoTe_2$ is beneficial to the modulation between them. In addition, the dichalcogenides of the transition metals such as Ti, Cr, Ni, Zn, V, Nb, and Ta just exhibit simple metal behavior [6]. 2H structure involves the hexagonal group (group name: P63/ MMC); the hexagonal lattice consists of two alternating sulfur atoms and a transition metal atom. Although most of 2H structures exhibit semiconductor properties in layer TMDCs, very few 2H phases exhibit metal behavior, such as 2H-NbS_2, 2H-$NbSe_2$, 2H-TaS_2, and 2H-$TaSe_2$ [183, 184].

The primary structure of metallic-layered TMD is 1T phase that belongs to the hexagonal basis. Due to the rotation of one tetrahedron, the resulting structure is an octahedron.

The dimerization of the transition metal atoms causes the distortion of the 1T structure to form the 1T' phase, especially the displacement in an out-of-plane direction and a symmetry transformation of chalcogen atoms. The difference

between 1T and TD is C-axis angle ($\alpha \neq 90$, $\beta = 90$). The 3R phase consists of three layers in one unit cell. For example, NbS_2, $NbSe_2$, TaS_2, and $TaSe_2$ appear in the H and T phases, as well as in the 3R phases [186].

Due to the diversity of its chemical composition and structural phases, TMD has a wide range of electrical properties, such as band structure characteristics (metal or insulation) and the appearance of correlated and topological phases.

The bulk phases of TMDCs are indirect bandgap.

Most of the semiconductor-layered TMDCs such as MoS_2 (1.8 eV), $MoSe_2$ (1.5 eV), (2H)-$MoTe_2$ (1.1 eV), WS_2 (2.1 eV), and WSe_2 (1.7 eV) exhibit direct bandgap in monolayer, whereas their bulk phases are indirect bandgap except a few cases such as GaSe and ReS_2 [187, 188]. The formation of TMDCs by the combination of Mo, W, S, and Se with VI group transition metals is discussed. MoS_2, WS_2, and WSe_2 display semiconducting properties in their thermodynamically stable 2H phase that drew attention to the application for electronic devices [11].

According to the first principle (density functional theory), the band structure of 2H-MoS_2 evolved from the bulk to monolayer is shown in Figure 1.5. With the thickness of 2H-MoS_2 decreasing, the upshift of valence band edge and the downshift of conduction band edge changes, and the indirect bandgap semiconductor block material is transformed into direct bandgap semiconductor monolayer material. The bulk and monolayer 2H-MoS_2 display bandgap values of 0.88 and 1.71 eV, respectively. The experimental bandgap of 2H-MoS_2 monolayer is 2.16 eV [189].

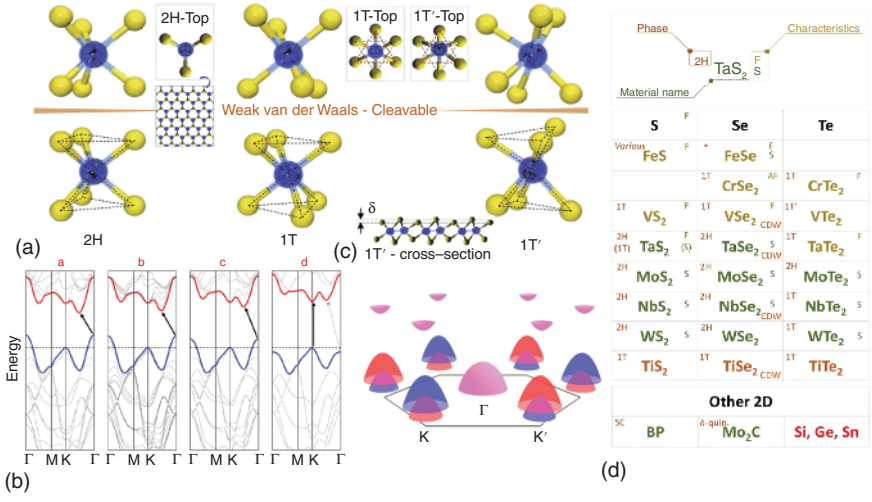

Figure 1.5 (a) 2H, 1T, 1T′ structures schematic diagram of layer TMDCs. *Source:* [180], © Materials Today 2017; (b) the band structure of 2H-MoS_2 changes from bulk to monolayer. *Source:* [166], © Nano letters 2010; (c) schematic illustration of the electronic band structure of monolayer TMD materials. *Source:* [185], © Physical Review B; (d) various physical properties such as magnetism (ferromagnetic is abbreviated to F in the table and antiferromagnetic is abbreviated to AF in the table), superconductivity (S in the table), charge density wave (CDW in the table), and corresponding crystal structures (2H, 1T) of various 2D TMD and other 2D materials. *Source:* [180], © Materials Today 2017.

Importantly, the maximum value of the valence band and the minimum value of the conduction band are located at two unequal points of high symmetry, K and K′, which correspond to the corners of the hexagonal Brillouin zone. Monolayer 2H-MoS_2 along with other group VI monolayers 2H-TMDCs and graphene have this property commonly and could realize the observation of valley-related physical phenomena and potential valley electronics applications.

1.2.5 Transition Metal Carbides (TMCs)

Transition metal carbides (TMCs) have a high conductivity, good hydrophilicity, and various surface terminations that are applied in the fields of electrogenerated chemiluminescence, catalysts, biosensors, anti-pollution and anti-bacterial agents, and biological detection [190–192]. Their good stability at high temperature also shows adequate reproducibility. Therefore, there is a high demand for TMCs, such as two-dimensional (2D) form (MXene), nanocomposites, nanoparticles, carbide films, carbide nanopowders, and carbide nanofibers. [193, 194]

MXene was first reported in 2011, after that, 70 different MXenes such as Ti_2CT_x, $Ti_3C_2T_x$, and $Nb_4C_3T_x$ have been synthesized, most of which belong to the 2D class of carbides [195]. Considering that over 100 stoichiometric structures have been predicted and can produce an infinite number of solid solutions, MXene is likely to be the largest 2D material family known to date.

$Mn_{+1}X_nT_x$ is the general formula of MXenes (M = early transition metal, X = carbon/nitrogen, $n = 1, 2, 3, 4$, T_x = surface terminations such as -OH, -F, -O) (Figure 1.6). MAX is the precursor of Mxenes where A is element of IIIA or IVA. By the etching "A" layer from MAX (the precursor of MXene, having the general formula $M_{n+1}AX_n$, A = aluminum) the MXenes are formed. The elements to form MAX phases, MXenes, and intercalated ions are shown in Figure 1.6. [197]

Most MXenes are carbides containing only one metallic element such as Ti_3C_2, Ti_4C_3, VC_2, and V_4C_3 [198]. Besides, binary metal carbides are also reported and two kinds of metals are located on the surface and in the middle of the MXenes, respectively (Mo_2TiC_2 or $Mo_2Ti_2C_3$) [199, 200]. Predictable compositions of Mxenes are greatly increased due to the abundant surface teminals, such as -O, -OH, -F, -Cl, -Br, and -S. Futhermore, the physical and chemical properties can be tuned by the surface terminals [196, 201]. For example, Wu has synthesized 2D MoS_2/Ti_3C_2 composite with surface terminations to provide edge-active sites for hydrogen evolution reaction (HER). The oxygen termination and hydronium ions bond/debond with each other in the acid media properly to effect the oxidation process during the charging and discharging process that improves the pseudo-capacitance.

Ordered phases and solid solutions are two different forms of MXenes. The transition metals are arranged randomly in solid solutions, while one transition metal layer lies between the layers of another transition metal in the ordered phase [193].

Except for the pure metal and carbon phases, the phases formed in the TMC system can be categorized as Hägg carbides (interstitial carbides). In Hägg carbides, a tightly stacked sequence was formed by metal atoms and the carbon atoms in Mxenes occupy the most (octahedral) interstices. All phases often appear to contain

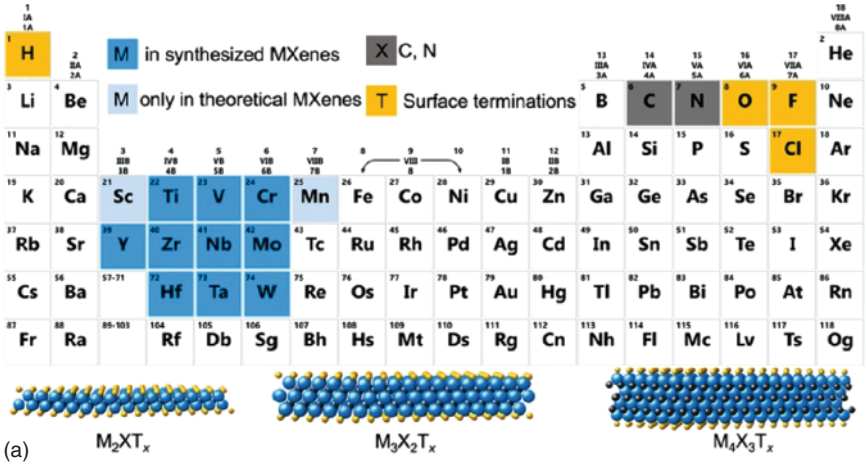

(a)

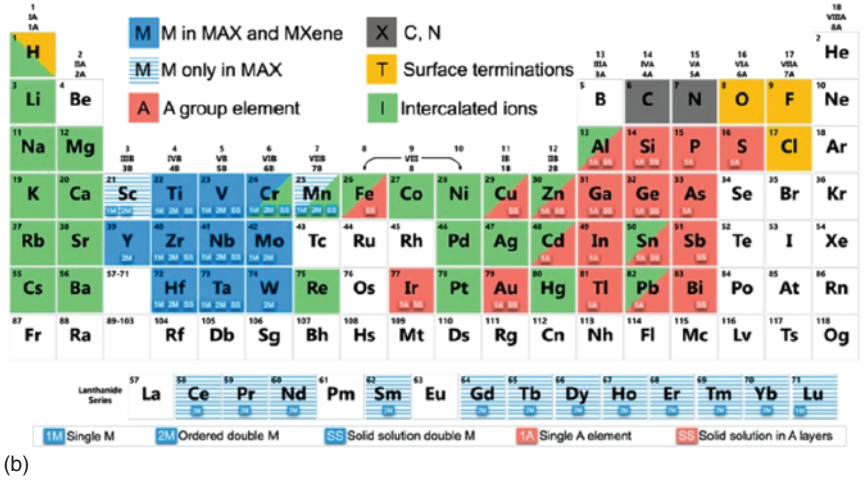

(b)

Figure 1.6 Compositions of MXenes and MAX phases in periodic tables. (a) Elements contained in MXenes. The bright blue elements represent MXenes that have not been yet experimentally confirmed. Schematic diagrams of three typical MXene structures are shown at the bottom; (b) elements used to build MAX phases, MXenes, and their intercalated ions. Elements with blue striped background have only been reported in Mxenene precursors (MAXC phase), and their Mxenes have not yet been synthesized. The element on the red background is element A in the MAX phase, which can be selectively etched into Mxenes. The green background shows the cations that have been intercalated into MXenes to date. According to the legend below, 1M and 1A represent the formation possibilities of a single (pure) transition metal and An element Max phase (and Mxene)1M and 1A indicate the formation possibility of a single (pure) transition metal and An element MAX phase (and MXene). SS indicates the existence of solid solutions in transition metal atomic planes (blue) or element planes (red); 2M indicates the possibility of the formation of ordered double transition metal Max phase or MXene (either in-plane or out-of-plane). *Source:* [196]. © ACS nano 2019.

a large number of nonstoichiometric components that are classified as strongly nonstoichiometric compounds [202].

Face-centered cubic (FCC) sublattice is always formed by metal atoms in the group IVB carbides. While on the other hand, the FCC sublattices are maintained only to the extent that the homogeneity of transition metals and carbon is approximately equal. When the ratio of metal:carbon approaches 2 : 1, which is M_2C, a hexagonal, tightly packed sublattice was formed by metal atoms. Between these two components, the VB group of carbides may form a mixture of FCC and hexagonal close-packed sequences of metal atoms, which are often indicated as the Zeta (f) phase.

Carbon sublattices offer the possibility of another set of phases, which is also very significant.

It is equally important to consider the carbon sublattice, which provides another interesting set of phase possibilities. The metal sublattice, chemical composition, and the temperature are factors that control the nonmetal sublattice.

In the case of equal amounts of metal and carbon, the B1(rock salt) structure is formed by filling all the octahedral gaps of the FCC metal sublattice with the carbon atoms.

Whereas, in substoichiometry, the actual chemical content and temperature affect the order arrangement of carbon atoms filling the octahedral gap.

Therefore, deviations from local stoichiometry tend to change the structure of carbon sublattices, whereas metal sublattices changing requires a dramatic change in stoichiometry.

Carbon sublattices act as solid solutions between carbon atoms, and structural vacancies should also be considered. This is important because the interaction between chemistry and structure is emphasized; furthermore, the potential of carbon sublattices to arrange themselves in an orderly manner at lower temperatures is also mentioned. Here, we briefly introduce the different structures of MX, M_6C_5, M_4C_3, M_3C_2, and M_2C.

MX crystal structure have a stoichiometry of 1:1. The metal atoms occupy an FCC lattice, while all the octahedral interstitials are occupied by the carbon atoms. This rock salt (B_1) phase exists in the carbide of IVB and VB groups, and they are stable in the temperature range from room temperature to the melting point.

When the carbon in B_1 structure is slightly lost, vacancy-ordered structures such as the M_6C_5 composition could be predicted. The V_8C_7 structure has also been reported in some cases. As the number of carbon lost is more, there are two kinds of structure near the ideal compositions of M_4C_3 or M_3C_2: (i) B1 structure with vacancy-ordered forms and (ii) phases with mixed FCC/hexagonal close-packed metal atom stacking sequences (also called stacking fault phases). Stable M_2C crystal structures has been achieved with the carbon depletion sufficiently, either as a vacancy-ordered form of the B_1 structure that is normally present in the group IVB carbides or as a structure based on a hexagonal close-packed arrangement of the metal atoms with the carbon atoms occupying the octahedral interstices as observed in the group VB carbides. As been reported, for the vacancy-ordered forms of the B1 structure, the vacancies on the M2C component can be arranged in a variety of ways [203].

1.2.6 Transition Metal Oxides (TMOs)

In comparison with other atomic thin materials, transition metal oxides (TMOs) have a relatively long usage history. They contain many of the earth's rich minerals and have been used for thousands of years as building materials, thermal treatment, pigments, lubricants, and many other applications. TMOs are composed of transition metals in the D region of the periodic table and oxygen. TMOs have the ability to change their bond structure and thus change their oxidation state, depending on the particularity of their chemical composition and crystal structure and are relatively easy to cause oxygen defects. Two-dimensional (2D) TMOs usually exhibit different physical and chemical properties compared to their bulk bodies. These differences increase the excellent properties, including the electronic properties of high-temperature superconductivity and multiferroicity, as well as the unique optical, mechanical, and thermal phenomena. Besides, the catalytic and chemical properties of TMOs can be changed by reducing their thickness. These properties result in potential applications that have been realized in the fields of optics, electronics, catalysis, energy components, sensors, and biological systems. Other emerging applications have been proven in piezoelectric, thermal elements, and superconductors [8, 204–206].

The unique characteristics of oxygen ions is the critical factor to produce excellent performance on the surface of TMOs, and especially for 2D TMOs, this surface performance dominates the performance of the material [207]. O^{2-} ions have strong polarization. This polarization allows the planar TMO to exhibit a large, nonlinear, and uneven charge distribution within its crystal lattice, resulting in electrostatic shielding on the length scale of 1–100 nm, resulting in an excellent local surface and interface features. Therefore, the specific energy state exists near or on the surface of planar TMOs, which are quite different from their bulk state, and also causes strong Coulomb interactions between the 2D TMOs and adjacent ions [208]. If surfaces of two TMOs are close to each other, a built-in interface potential can be generated, changing the Fermi level of the surface plane that will significantly affect its electronic properties. In this type of planar TMOs, different atomic orbitals may contribute to the electronic states. The surface of TMOs can also be activated by electrons due to the hybridization of ion orbitals. If the D orbits of 2D TMO are perpendicular to their plane arrangement, the orbital order and spin order may be frustrated or generated [205, 207]. This creates unconventional semiconductor characteristics.

There are many kinds of transition metals that can be used to form TMOs. Many basic properties of TMOs depend on the types of cations and their flexibility to change the oxidation state. Especially in 2D TMOs, a large number of structures can only be stabilized by cations with different charge states and binding configurations [209]. For the same TMO layer under different stoichiometric ratios, the various electronic properties of metal to wide gap insulation behavior are caused by different metal oxidation states. The metal-insulator phase transition as a function of pressure and temperature is caused by the local properties of the d electronic state. 2D TMOs have a variety of bandgaps, providing the possibility to adjust optical

and electrical properties at almost any wavelength [205]. Nanostructured TMOs have unique redox characteristics, many of which show a reversible trend. Excellent chemical and thermal stability is also possessed by many 2D TMOs [210]. The oxygen vacancies in nanostructured TMO can be changed by various mature procedures to achieve significant tunability [211]. Furthermore, the surface chemistry and bulk structure of 2D TMOs are significantly different due to the decrease of oxygen vacancy formation energy and the increase of reducibility of metal cations [212].

According to the structure of the 2D TMOs source matrix crystal, it is mainly divided into two types: layer structured and nonlayer structured TMOs [213]. Layer structured TMOs such as MoO_3, WO_3, Ga_2O_3, and V_2O_5 can exist naturally in the form of layered crystals in hydrate or anhydrous phase. In their corresponding 3D matrix, the atoms in-plane of the same layer are covalently bonded, and the layers are combined by weak interaction force between the stacking directions of the layers. These oxides can be exfoliated into nanosheets with oxygen terminated substrate surface by liquid or gas phase technology, which remain stable in air and water. These TMOs can be reduced to layers, the number of which is in the thinnest and most stable planar configuration, depending on their unit cell composition.

Among them, binary metal trioxides have a layered structure with a general formula of MO_3 (M = Mo, Ta, W, etc.) [206, 214]. For example, each layer in layered MoO_3 (Figure 1.7a) is mainly composed of deformed MoO_6 octahedrons in orthorhombic crystals [215]. The 2D layer is formed by octahedron and its neighbors sharing edges. The bulk crystal is formed by stacking the layers in turn along the y-axis by vdW force. Another typical layered TMO material is V_2O_5 (Figure 1.7b). The α-V_2O_5 is the most stable phase in the vanadium oxide family because it has the

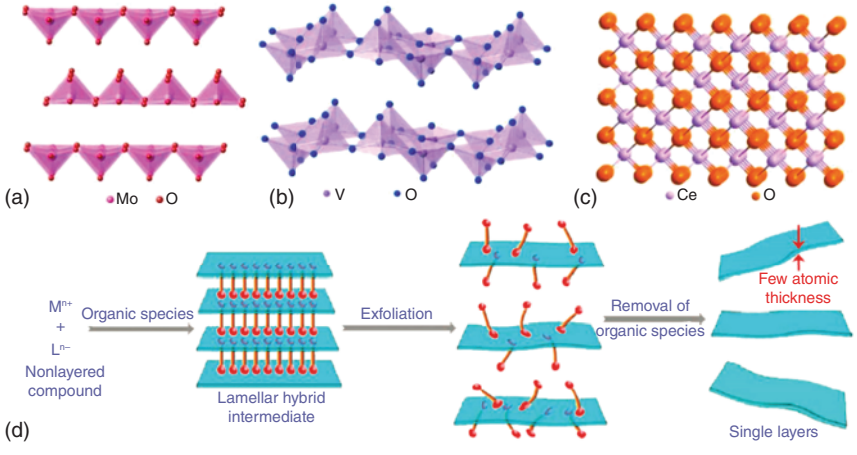

Figure 1.7 (a) Crystal structures of MoO_3; (b) crystal structures of V_2O_5; (c) crystal structures of CeO_2. *Source:* Reproduced with permission from Ref. [213], © Chemical Reviews 2017; (d) schematic drawing of the preparation of nonlayered structures into nanosheets. *Source:* Reproduced with permission from Ref. [215], © Nature Communications 2012.

highest vanadium oxidation state. It has a layered structure and a positive cross-cell structure during crystallization [216]. The monolayer consists of a twisted triangular biconical polyhedron with O atoms around V atoms. The polyhedron forms a $(V_2O_4)_n$ zigzag double chain along the direction (001), sharing edges and cross-linking edges along the direction (100), forming a 2D layer. The layers are also stacked together by vdW force to form bulk crystals.

Among the currently known TMO materials, only a few have a layered structure, and most of them are nonlayered structures in which atoms are connected by chemical bonds in the 3D direction of the crystal [217]. Some common nonlayer structured TMOs are CeO_2, TiO_2, In_2O_3, HfO_2, and Fe_2O_3. Most of their crystal structures are different from each other, so there is no general formula [218]. CeO_2 is one example of nonlayer structured TMOs. CeO_2 has a fluorite structure and the space group is Fm3m (Figure 1.7c). Fluorite structure is formed on the basis of FCC unit cell, in which cations and anions occupy octahedral space. In the CeO_2 structure, each Ce^{4+} ion coordinates with eight equivalent O^{2-} nearest neighbors, while each O^{2-} ion coordinates with four nearest neighbors Ce^{4+} [78]. There is no obvious natural delamination inside the crystal of the material, so it cannot be separated by methods such as micromechanical exfoliation. However, if the vertical chemical bonds inside the crystal are broken, the thickness of the crystal is reduced to an atomic size and a 2D plane with a certain lateral size appears, then 2D TMOs different from the corresponding parent crystal can be obtained (Figure 1.7d).

Compared with layer structured TMOs, nonlayer structured TMOs combine the advantages of an atomically thin structure and a highly active surface and also produce many new characteristics. When the structure of the material changes from a 3D bulk to a 2D layer with an atomic thickness of only a few nanometers, the sharp decrease in the thickness causes the distortion of the material lattice structure, and finally a stable structure with a lower surface energy is formed. The reconstruction of crystal structure will also lead to the change of energy band structure and electronic state [219]. Due to the breaking of the chemical bonds in the vertical direction of the 3D matrix, a large number of unsaturated dangling bonds are generated on the newly formed surface. Together with the strong surface polarization, a highly active surface with many active sites and a large specific surface area is formed [218], making it expected to have high-efficiency catalytic ability and energy storage performance. In addition, the 2D planar structure makes 2D nonlayer structured TMOs compatible with microelectronic technology processing [220]. It can overcome the shortcomings of the high rigidity of traditional semiconductor materials such as silicon, making it expected to be widely used in the emerging flexible electronic fields such as wearable technology.

Different methods have been designed to synthesize 2D TMOs based on gas phase and liquid phase processes. It is still a challenging task to precisely synthesize inorganic planar crystals of one or more unit thickness during gas phase synthesis. Layer by layer epitaxy of two-dimensional films is classified as Frank van der Merwe growth [221]. For TMOs, the flux of adsorbed atoms and the lowest unfilled surface energy of the substrate on which the new material is deposited determine the occurrence of layer by layer oxide epitaxy [222]. For the physical deposition in the vapor phase, in a small period superlattice, one or more cell surfaces may grow

independently or in combination. The most common 2D TMO vapor phase techniques include CVD, MBE, atomic layer deposition (ALD), and pulsed laser deposition (PLD). In order to successfully deposit atomic-scale thin oxide layer or superlattice, it is necessary to precisely adjust deposition parameters. Especially in MBE, 2D deposition needs to significantly reduce the flux of adsorbed atoms, so it usually needs ultrahigh vacuum environment, which increases the complexity of equipment and deposition cost. Another problem is the influence of the substrate on the perfect deposition of oxides. The lattice matching and surface energy factors should be considered at the same time.

Many current 2D TMO synthesis techniques rely on liquid phase environments. Oxide epitaxial layers can be solvothermally grown in liquid solutions (at elevated temperatures) with or without a guiding agent [218, 223]. The carrier solvent can be water based and depends on the evaporation temperature of the solution, which may be necessary to be carried out in a pressurized container. The purity of the analyte and solvent plays an important role in the final result. Solution-based technology can be performed in one step, forming a layer directly on the substrate. Similar to the vapor deposition technique, it is important to consider the registration of the unit cell and the substrate or the layers near it for the nonscattering displacement and exchange of free carriers. The crystal orientation should be controlled at the cell level in these cases, and other quasi liquid methods may also be applied. The precursor of the material can be obtained by secondary processes such as spin coating, dip coating, or drop casting, such as oxygen annealing.

If the products synthesized in liquid or gas phase are layered crystals, the number of layers can be reduced by using the exfoliation step. These layered crystals can form different material patterns between TMO planes. After the exfoliation is completed, the pattern can be left to stabilize the oxide layer or be removed [224].

References

1 Castro Neto, A.H., Guinea, F., Peres, N.M.R. et al. (2009). The electronic properties of graphene. *Reviews of Modern Physics* 81: 109–162.

2 Novoselov, K.S., Geim, A.K., Morozov, S.V. et al. (2004). Electric field effect in atomically thin carbon films. *Science* 306: 666.

3 Schmidt, H., Giustiniano, F., and Eda, G. (2015). Electronic transport properties of transition metal dichalcogenide field-effect devices: surface and interface effects. *Chemical Society Reviews* 44: 7715–7736.

4 Duan, X., Wang, C., Pan, A. et al. (2015). Two-dimensional transition metal dichalcogenides as atomically thin semiconductors: opportunities and challenges. *Chemical Society Reviews* 44: 8859–8876.

5 Xie, L.M. (2015). Two-dimensional transition metal dichalcogenide alloys: preparation, characterization and applications. *Nanoscale* 7: 18392–18401.

6 Wang, Q.H., Kalantar-Zadeh, K., Kis, A. et al. (2012). Electronics and optoelectronics of two-dimensional transition metal dichalcogenides. *Nature Nanotechnology* 7: 699–712.

7 Chhowalla, M., Shin, H.S., Eda, G. et al. (2013). The chemistry of two-dimensional layered transition metal dichalcogenide nanosheets. *Nature Chemistry* 5: 263–275.

8 Butler, S.Z., Hollen, S.M., Cao, L. et al. (2013). Progress, Challenges, and Opportunities in Two-Dimensional Materials Beyond Graphene. *ACS Nano* 7: 2898–2926.

9 Xu, M., Liang, T., Shi, M., and Chen, H. (2013). Graphene-like two-dimensional materials. *Chemical Reviews* 113: 3766–3798.

10 Ci, L., Song, L., Jin, C. et al. (2010). Atomic layers of hybridized boron nitride and graphene domains. *Nature Materials* 9: 430–435.

11 Radisavljevic, B., Radenovic, A., Brivio, J. et al. (2011). Single-layer MoS_2 transistors. *Nature Nanotechnology* 6: 147–150.

12 Zhang, H., Liu, C.-X., Qi, X.-L. et al. (2009). Topological insulators in Bi_2Se_3, Bi_2Te_3 and Sb_2Te_3 with a single Dirac cone on the surface. *Nature Physics* 5: 438–442.

13 Liu, Y., Weiss, N.O., Duan, X. et al. (2016). Van der Waals heterostructures and devices. *Nature Reviews Materials* 1: 16042.

14 Jariwala, D., Sangwan, V.K., Lauhon, L.J. et al. (2014). Emerging device applications for semiconducting two-dimensional transition metal dichalcogenides. *ACS Nano* 8: 1102–1120.

15 Huang, X., Zeng, Z., and Zhang, H. (2013). Metal dichalcogenide nanosheets: preparation, properties and applications. *Chemical Society Reviews* 42: 1934–1946.

16 Huang, X., Tan, C., Yin, Z., and Zhang, H. (2014). 25th anniversary article: hybrid nanostructures based on two-dimensional nanomaterials. *Advanced Materials* 26: 2185–2204.

17 Li, H., Wu, J., Yin, Z., and Zhang, H. (2014). Preparation and applications of mechanically exfoliated single-layer and multilayer MoS_2 and WSe_2 nanosheets. *Accounts of Chemical Research* 47: 1067–1075.

18 Chen, Y.L., Analytis, J.G., Chu, J.H. et al. (2009). Experimental realization of a three-dimensional topological insulator, Bi_2Te_3. *Science* 325: 178.

19 Zeng, M., Xiao, Y., Liu, J. et al. (2018). Exploring two-dimensional materials toward the next-generation circuits: from monomer design to assembly control. *Chemical Reviews* 118: 6236–6296.

20 Wang, H., Yuan, H., Sae Hong, S. et al. (2015). Physical and chemical tuning of two-dimensional transition metal dichalcogenides. *Chemical Society Reviews* 44: 2664–2680.

21 Fan, J., Li, T., and Djerdj, I. (2015). Two-dimensional atomic crystals: paving new ways for nanoelectronics. *Journal of Electronic Materials* 44: 4080–4097.

22 Parviz, B.A., Ryan, D., and Whitesides, G.M. (2003). Using self-assembly for the fabrication of nano-scale electronic and photonic devices. *IEEE Transactions on Advanced Packaging* 26: 233–241.

23 Voiry, D., Mohite, A., and Chhowalla, M. (2015). Phase engineering of transition metal dichalcogenides. *Chemical Society Reviews* 44: 2702–2712.

24 Das, S., Robinson, J.A., Dubey, M. et al. (2015). Beyond graphene: progress in novel two-dimensional materials and van der Waals solids. *Annual Review of Materials Research* 45: 1–27.

25 Coleman, J.N., Lotya, M., O'Neill, A. et al. (2011). Two-dimensional nanosheets produced by liquid exfoliation of layered materials. *Science* 331: 568.

26 Wilson, J.A. and Yoffe, A.D. (1969). The transition metal dichalcogenides discussion and interpretation of the observed optical, electrical and structural properties. *Advances in Physics* 18: 193–335.

27 Taha-Tijerina, J., Narayanan, T.N., Gao, G. et al. (2012). Electrically insulating thermal nano-oils using 2D fillers. *ACS Nano* 6: 1214–1220.

28 Lin, S.S. (2012). Light-emitting two-dimensional ultrathin silicon carbide. *The Journal of Physical Chemistry C* 116: 3951–3955.

29 Yang, S., Gong, Y., Liu, Z. et al. (2013). Bottom-up approach toward single-crystalline VO_2-graphene ribbons as cathodes for ultrafast lithium storage. *Nano Letters* 13: 1596–1601.

30 Kong, D., Dang, W., Cha, J.J. et al. (2010). Few-layer nanoplates of Bi_2Se_3 and Bi_2Te_3 with highly tunable chemical potential. *Nano Letters* 10: 2245–2250.

31 Zhang, H. (2015). Ultrathin two-dimensional nanomaterials. *ACS Nano* 9: 9451–9469.

32 Morozov, S.V., Novoselov, K.S., Katsnelson, M.I. et al. (2008). Giant intrinsic carrier mobilities in graphene and its bilayer. *Physical Review Letters* 100: 016602.

33 Balandin, A.A., Ghosh, S., Bao, W. et al. (2008). Superior thermal conductivity of single-layer graphene. *Nano Letters* 8: 902–907.

34 Zhu, Y., Murali, S., Cai, W. et al. (2010). Graphene and graphene oxide: synthesis, properties, and applications. *Advanced Materials* 22: 3906–3924.

35 Banszerus, L., Schmitz, M., Engels, S. et al. (2015). Ultrahigh-mobility graphene devices from chemical vapor deposition on reusable copper. *Science Advances* 1: e1500222.

36 Lee, C., Wei, X., Kysar, J.W., and Hone, J. (2008). Measurement of the elastic properties and intrinsic strength of monolayer graphene. *Science* 321: 385.

37 Hirsch, A. (2010). The era of carbon allotropes. *Nature Materials* 9: 868–871.

38 Kim, B.G. and Choi, H.J. (2012). Graphyne: hexagonal network of carbon with versatile dirac cones. *Physical Review B* 86: 115435.

39 Long, M., Tang, L., Wang, D. et al. (2011). Electronic structure and carrier mobility in graphdiyne sheet and nanoribbons: theoretical predictions. *ACS Nano* 5: 2593–2600.

40 Yang, N., Liu, Y., Wen, H. et al. (2013). Photocatalytic properties of graphdiyne and graphene modified TiO_2: from theory to experiment. *ACS Nano* 7: 1504–1512.

41 Cranford, S.W., Brommer, D.B., and Buehler, M.J. (2012). Extended graphynes: simple scaling laws for stiffness, strength and fracture. *Nanoscale* 4: 7797–7809.

42 Li, J., Xie, Z., Xiong, Y. et al. (2017). Architecture of β-graphdiyne-containing thin film using modified Glaser–Hay coupling reaction for enhanced photocatalytic property of TiO_2. *Advanced Materials* 29: 1700421.

43 Li, G., Li, Y., Liu, H. et al. (2010). Architecture of graphdiyne nanoscale films. *Chemical Communications* 46: 3256–3258.

44 Li, J., Gao, X., Liu, B. et al. (2016). Graphdiyne: a metal-free material as hole transfer layer to fabricate quantum dot-sensitized photocathodes for hydrogen production. *Journal of the American Chemical Society* 138: 3954–3957.

45 Zhou, J., Gao, X., Liu, R. et al. (2015). Synthesis of graphdiyne nanowalls using acetylenic coupling reaction. *Journal of the American Chemical Society* 137: 7596–7599.

46 Sun, Q., Cai, L., Ma, H. et al. (2016). Dehalogenative homocoupling of terminal alkynyl bromides on Au(111): incorporation of acetylenic scaffolding into surface nanostructures. *ACS Nano* 10: 7023–7030.

47 Matsuoka, R., Sakamoto, R., Hoshiko, K. et al. (2017). Crystalline graphdiyne nanosheets produced at a gas/liquid or liquid/liquid interface. *Journal of the American Chemical Society* 139: 3145–3152.

48 Li, Y., Xu, L., Liu, H., and Li, Y. (2014). Graphdiyne and graphyne: from theoretical predictions to practical construction. *Chemical Society Reviews* 43: 2572–2586.

49 Tang, H., Hessel, C.M., Wang, J. et al. (2014). Two-dimensional carbon leading to new photoconversion processes. *Chemical Society Reviews* 43: 4281–4299.

50 Malko, D., Neiss, C., Viñes, F., and Görling, A. (2012). Competition for graphene: graphynes with direction-dependent dirac cones. *Physical Review Letters* 108: 086804.

51 Nulakani, N.V.R. and Subramanian, V. (2016). A theoretical study on the design, Structure, and Electronic Properties of Novel Forms of Graphynes. *The Journal of Physical Chemistry C* 120: 15153–15161.

52 Kuang, C., Tang, G., Jiu, T. et al. (2015). Highly efficient electron transport obtained by doping PCBM with graphdiyne in planar-heterojunction perovskite solar cells. *Nano Letters* 15: 2756–2762.

53 Noguchi, E., Sugawara, K., Yaokawa, R. et al. (2015). Direct observation of dirac cone in multilayer silicene intercalation compound $CaSi_2$. *Advanced Materials* 27: 856–860.

54 Nakano, H., Ishii, M., and Nakamura, H. (2005). Preparation and structure of novel siloxene nanosheets. *Chemical Communications* 2005: 2945–2947.

55 Nakano, H., Mitsuoka, T., Harada, M. et al. (2006). Soft synthesis of single-crystal silicon monolayer sheets. *Angewandte Chemie International Edition* 45: 6303–6306.

56 Fan, Z., Huang, X., Han, Y. et al. (2015). Surface modification-induced phase transformation of hexagonal close-packed gold square sheets. *Nature Communications* 6: 6571.

57 De Padova, P., Quaresima, C., Ottaviani, C. et al. (2010). Evidence of graphene-like electronic signature in silicene nanoribbons. *Applied Physics Letters* 96: 261905.

58 Rachid Tchalala, M., Enriquez, H., Mayne, A.J. et al. (2013). Formation of one-dimensional self-assembled silicon nanoribbons on Au(110)-(2×1). *Applied Physics Letters* 102: 083107.

59 Fan, Z., Bosman, M., Huang, X. et al. (2015). Stabilization of 4H hexagonal phase in gold nanoribbons. *Nature Communications* 6: 7684.

60 Chiappe, D., Scalise, E., Cinquanta, E. et al. (2014). Two-dimensional Si nanosheets with local hexagonal structure on a MoS_2 surface. *Advanced Materials* 26: 2096–2101.

61 Zhao, J., Deng, Q., Bachmatiuk, A. et al. (2014). Free-standing single-atom-thick iron membranes suspended in graphene pores. *Science* 343: 1228.

62 Volders, C., Monazami, E., Ramalingam, G., and Reinke, P. (2017). Alternative route to silicene synthesis via surface reconstruction on h-$MoSi_2$ crystallites. *Nano Letters* 17: 299–307.

63 Liu, C.-C., Feng, W., and Yao, Y. (2011). Quantum spin hall effect in silicene and two-dimensional germanium. *Physical Review Letters* 107: 076802.

64 Sun, J.-T., Wang, Z., Meng, S. et al. (2016). Spin-polarized valley Hall effect in ultrathin silicon nanomembrane via interlayer antiferromagnetic coupling. *2D Materials* 3: 035026.

65 Pal, M., Pal, U., Jiménez, J.M.G.Y., and Pérez-Rodríguez, F. (2012). Effects of crystallization and dopant concentration on the emission behavior of TiO_2:Eu nanophosphors. *Nanoscale Research Letters* 7: 1.

66 Zhang, C.-w. and Yan, S.-s. (2012). First-principles study of ferromagnetism in two-dimensional silicene with hydrogenation. *The Journal of Physical Chemistry C* 116: 4163–4166.

67 Guo, Y., Zhou, S., Bai, Y., and Zhao, J. (2016). Tunable thermal conductivity of silicene by germanium doping. *Journal of Superconductivity and Novel Magnetism* 29: 717–720.

68 Zhang, R.-w., Zhang, C.-w., Li, S.-s. et al. (2014). Design of half-metallic ferromagnetism in germanene/silicene hybrid sheet. *Solid State Communications* 191: 49–53.

69 Morishita, T., Russo, S.P., Snook, I.K. et al. (2010). First-principles study of structural and electronic properties of ultrathin silicon nanosheets. *Physical Review B* 82: 045419.

70 Kim, W.-S., Hwa, Y., Shin, J.-H. et al. (2014). Scalable synthesis of silicon nanosheets from sand as an anode for Li-ion batteries. *Nanoscale* 6: 4297–4302.

71 Derivaz, M., Dentel, D., Stephan, R. et al. (2015). Continuous germanene layer on Al(111). *Nano Letters* 15: 2510–2516.

72 Dávila, M.E., Xian, L., Cahangirov, S. et al. (2014). Germanene: a novel two-dimensional germanium allotrope akin to graphene and silicene. *New Journal of Physics* 16: 095002.

73 Golias, E., Xenogiannopoulou, E., Tsoutsou, D. et al. (2013). Surface electronic bands of submonolayer Ge on Ag(111). *Physical Review B* 88: 075403.

74 O'Hare, A., Kusmartsev, F.V., and Kugel, K.I. (2012). A stable "Flat" form of two-dimensional crystals: could graphene, silicene, germanene be minigap semiconductors? *Nano Letters* 12: 1045–1052.

75 Houssa, M., Pourtois, G., Afanas'ev, V.V., and Stesmans, A. (2010). Electronic properties of two-dimensional hexagonal germanium. *Applied Physics Letters* 96: 082111.

76 Pulci, O., Marsili, M., Garbuio, V. et al. (2015). Excitons in two-dimensional sheets with honeycomb symmetry. *Physica Status Solidi (b)* 252: 72–77.

77 Pulci, O., Gori, P., Marsili, M. et al. (2012). Strong excitons in novel two-dimensional crystals: silicane and germanane. *EPL (Europhysics Letters)* 98: 37004.

78 Ye, X.-S., Shao, Z.-G., Zhao, H. et al. (2014). Intrinsic carrier mobility of germanene is larger than graphene's: first-principle calculations. *RSC Advances* 4: 21216–21220.

79 Dávila, M.E. and Le Lay, G. (2016). Few layer epitaxial germanene: a novel two-dimensional Dirac material. *Scientific Reports* 6: 20714.

80 Zhang, L., Bampoulis, P., van Houselt, A., and Zandvliet, H.J.W. (2015). Two-dimensional Dirac signature of germanene. *Applied Physics Letters* 107: 111605.

81 Han, Y., Dong, J., Qin, G., and Hu, M. (2016). Phonon transport in the ground state of two-dimensional silicon and germanium. *RSC Advances* 6: 69956–69965.

82 Yan, J.-A., Stein, R., Schaefer, D.M. et al. (2013). Electron-phonon coupling in two-dimensional silicene and germanene. *Physical Review B* 88: 121403.

83 Huang, L.-F., Gong, P.-L., and Zeng, Z. (2015). Phonon properties, thermal expansion, and thermomechanics of silicene and germanene. *Physical Review B* 91: 205433.

84 Bishnoi, B. and Ghosh, B. (2013). Spin transport in silicene and germanene. *RSC Advances* 3: 26153–26159.

85 Zhang, R.-w., Ji, W.-x., Zhang, C.-w. et al. (2016). Controllable electronic and magnetic properties in a two-dimensional germanene heterostructure. *Physical Chemistry Chemical Physics* 18: 12169–12174.

86 Wei, W., Dai, Y., Huang, B., and Jacob, T. (2013). Many-body effects in silicene, silicane, germanene and germanane. *Physical Chemistry Chemical Physics* 15: 8789–8794.

87 Matthes, L., Gori, P., Pulci, O., and Bechstedt, F. (2013). Universal infrared absorbance of two-dimensional honeycomb group-IV crystals. *Physical Review B* 87: 035438.

88 Bechstedt, F., Matthes, L., Gori, P., and Pulci, O. (2012). Infrared absorbance of silicene and germanene. *Applied Physics Letters* 100: 261906.

89 Yang, K., Cahangirov, S., Cantarero, A. et al. (2014). Thermoelectric properties of atomically thin silicene and germanene nanostructures. *Physical Review B* 89: 125403.

90 Ni, Z., Liu, Q., Tang, K. et al. (2012). Tunable bandgap in silicene and germanene. *Nano Letters* 12: 113–118.

91 Zhang, R.-w., Ji, W.-x., Zhang, C.-w. et al. (2016). New family of room temperature quantum spin Hall insulators in two-dimensional germanene films. *Journal of Materials Chemistry C* 4: 2088–2094.

92 Ma, Y., Dai, Y., Niu, C., and Huang, B. (2012). Halogenated two-dimensional germanium: candidate materials for being of Quantum Spin Hall state. *Journal of Materials Chemistry* 22: 12587–12591.

93 Zhu, F.-f., Chen, W.-j., Xu, Y. et al. (2015). Epitaxial growth of two-dimensional stanene. *Nature Materials* 14: 1020–1025.

94 Tao, L., Yang, C., Wu, L. et al. (2016). Tension-induced mechanical properties of stanene. *Modern Physics Letters B* 30: 1650146.

95 Nissimagoudar, A.S., Manjanath, A., and Singh, A.K. (2016). Diffusive nature of thermal transport in stanene. *Physical Chemistry Chemical Physics* 18: 14257–14263.

96 Cherukara, M.J., Narayanan, B., Kinaci, A. et al. (2016). Ab initio-based bond order potential to investigate low thermal conductivity of stanene nanostructures. *The Journal of Physical Chemistry Letters* 7: 3752–3759.

97 Broek, B.v.d., Houssa, M., Scalise, E. et al. (2014). Two-dimensional hexagonal tin: ab initio geometry, stability, electronic structure and functionalization. *2D Materials* 1: 021004.

98 Houssa, M., van den Broek, B., Iordanidou, K. et al. (2016). Topological to trivial insulating phase transition in stanene. *Nano Research* 9: 774–778.

99 Rachel, S. and Ezawa, M. (2014). Giant magnetoresistance and perfect spin filter in silicene, germanene, and stanene. *Physical Review B* 89: 195303.

100 Shaidu, Y. and Akin-Ojo, O. (2016). First principles predictions of superconductivity in doped stanene. *Computational Materials Science* 118: 11–15.

101 Zhang, H., Zhang, J., Zhao, B. et al. (2016). Quantum anomalous Hall effect in stable dumbbell stanene. *Applied Physics Letters* 108: 082104.

102 Bridgman, P.W. (1916). Further note on black phosphorus. *Journal of the American Chemical Society* 38: 609–612.

103 Bridgman, P.W. (1914). Two new modifications of phosphorus. *Journal of the American Chemical Society* 36: 1344–1363.

104 Du, H., Lin, X., Xu, Z., and Chu, D. (2015). Recent developments in black phosphorus transistors. *Journal of Materials Chemistry C* 3: 8760–8775.

105 Balendhran, S., Walia, S., Nili, H. et al. (2015). Elemental analogues of graphene: silicene, germanene, stanene, and phosphorene. *Small* 11: 640–652.

106 Bhimanapati, G.R., Lin, Z., Meunier, V. et al. (2015). Recent advances in two-dimensional materials beyond graphene. *ACS Nano* 9: 11509–11539.

107 Dong, S., Zhang, A., Liu, K. et al. (2016). Ultralow-frequency collective compression mode and strong interlayer coupling in multilayer black phosphorus. *Physical Review Letters* 116: 087401.

108 Li, L., Yu, Y., Ye, G.J. et al. (2014). Black phosphorus field-effect transistors. *Nature Nanotechnology* 9: 372–377.

109 Engel, M., Steiner, M., and Avouris, P. (2014). Black phosphorus photodetector for multispectral, high-resolution imaging. *Nano Letters* 14: 6414–6417.

110 Yasaei, P., Kumar, B., Foroozan, T. et al. (2015). High-quality black phosphorus atomic layers by liquid-phase exfoliation. *Advanced Materials* 27: 1887–1892.

111 Kang, J., Wood, J.D., Wells, S.A. et al. (2015). Solvent exfoliation of electronic-grade, two-dimensional black phosphorus. *ACS Nano* 9: 3596–3604.

112 Hanlon, D., Backes, C., Doherty, E. et al. (2015). Liquid exfoliation of solvent-stabilized few-layer black phosphorus for applications beyond electronics. *Nature Communications* 6: 8563.

113 Zhang, S., Yang, J., Xu, R. et al. (2014). Extraordinary photoluminescence and strong temperature/angle-dependent Raman responses in few-layer phosphorene. *ACS Nano* 8: 9590–9596.

114 Sofer, Z., Sedmidubský, D., Huber, Š. et al. (2016). Layered black phosphorus: strongly anisotropic magnetic, electronic, and electron-transfer properties. *Angewandte Chemie International Edition* 55: 3382–3386.

115 Lin, S., Liu, S., Yang, Z. et al. (2016). Solution-processable ultrathin black phosphorus as an effective electron transport layer in organic photovoltaics. *Advanced Functional Materials* 26: 864–871.

116 Çakır, D., Sevik, C., and Peeters, F.M. (2015). Significant effect of stacking on the electronic and optical properties of few-layer black phosphorus. *Physical Review B* 92: 165406.

117 Peng, X., Wei, Q., and Copple, A. (2014). Strain-engineered direct-indirect band gap transition and its mechanism in two-dimensional phosphorene. *Physical Review B* 90: 085402.

118 Dai, J. and Zeng, X.C. (2014). Bilayer phosphorene: effect of stacking order on bandgap and its potential applications in thin-film solar cells. *The Journal of Physical Chemistry Letters* 5: 1289–1293.

119 Tahir, M., Vasilopoulos, P., and Peeters, F.M. (2015). Magneto-optical transport properties of monolayer phosphorene. *Physical Review B* 92: 045420.

120 Han, X., Stewart, H.M., Shevlin, S.A. et al. (2014). Strain and orientation modulated bandgaps and effective masses of phosphorene nanoribbons. *Nano Letters* 14: 4607–4614.

121 Tran, V., Soklaski, R., Liang, Y., and Yang, L. (2014). Layer-controlled band gap and anisotropic excitons in few-layer black phosphorus. *Physical Review B* 89: 235319.

122 Wei, Q. and Peng, X. (2014). Superior mechanical flexibility of phosphorene and few-layer black phosphorus. *Applied Physics Letters* 104: 251915.

123 Aierken, Y., Çakır, D., Sevik, C., and Peeters, F.M. (2015). Thermal properties of black and blue phosphorenes from a first-principles quasiharmonic approach. *Physical Review B* 92: 081408.

124 Wang, X., Jones, A.M., Seyler, K.L. et al. (2015). Highly anisotropic and robust excitons in monolayer black phosphorus. *Nature Nanotechnology* 10: 517–521.

125 Fei, R. and Yang, L. (2014). Strain-engineering the anisotropic electrical conductance of few-layer black phosphorus. *Nano Letters* 14: 2884–2889.

126 Guan, J., Zhu, Z., and Tománek, D. (2014). Phase coexistence and metal-insulator transition in few-layer phosphorene: a computational study. *Physical Review Letters* 113: 046804.

127 Zhu, Z. and Tománek, D. (2014). Semiconducting layered blue phosphorus: a computational study. *Physical Review Letters* 112: 176802.

128 Liu, Q., Zhang, X., Abdalla, L.B. et al. (2015). Switching a normal insulator into a topological insulator via electric field with application to phosphorene. *Nano Letters* 15: 1222–1228.

129 Tsai, H.-S., Wang, S.-W., Hsiao, C.-H. et al. (2016). Direct synthesis and practical bandgap estimation of multilayer arsenene nanoribbons. *Chemistry of Materials* 28: 425–429.

130 Zeraati, M., Vaez Allaei, S.M., Abdolhosseini Sarsari, I. et al. (2016). Highly anisotropic thermal conductivity of arsenene: an ab initio study. *Physical Review B* 93: 085424.

131 Zhang, H., Ma, Y., and Chen, Z. (2015). Quantum spin hall insulators in strain-modified arsenene. *Nanoscale* 7: 19152–19159.

132 Ares, P., Aguilar-Galindo, F., Rodríguez-San-Miguel, D. et al. (2016). Mechanical isolation of highly stable antimonene under ambient conditions. *Advanced Materials* 28: 6332–6336.

133 Gibaja, C., Rodriguez-San-Miguel, D., Ares, P. et al. (2016). Few-layer antimonene by liquid-phase exfoliation. *Angewandte Chemie International Edition* 55: 14345–14349.

134 Wu, X., Shao, Y., Liu, H. et al. (2017). Epitaxial growth and air-stability of monolayer antimonene on $PdTe_2$. *Advanced Materials* 29: 1605407.

135 Ji, J., Song, X., Liu, J. et al. (2016). Two-dimensional antimonene single crystals grown by van der Waals epitaxy. *Nature Communications* 7: 13352.

136 Yang, L., Song, Y., Mi, W., and Wang, X. (2016). The electronic structure and spin–orbit-induced spin splitting in antimonene with vacancy defects. *RSC Advances* 6: 66140–66146.

137 Gupta, S.K., Sonvane, Y., Wang, G., and Pandey, R. (2015). Size and edge roughness effects on thermal conductivity of pristine antimonene allotropes. *Chemical Physics Letters* 641: 169–172.

138 Hu, Y., Wu, Y., and Zhang, S. (2016). Influences of Stone–Wales defects on the structure, stability and electronic properties of antimonene: a first principle study. *Physica B: Condensed Matter* 503: 126–129.

139 Singh, D., Gupta, S.K., Sonvane, Y., and Lukačević, I. (2016). Antimonene: a monolayer material for ultraviolet optical nanodevices. *Journal of Materials Chemistry C* 4: 6386–6390.

140 Zhang, S., Yan, Z., Li, Y. et al. (2015). Atomically thin arsenene and antimonene: semimetal–semiconductor and indirect–direct band-gap transitions. *Angewandte Chemie International Edition* 54: 3112–3115.

141 Wang, G., Pandey, R., and Karna, S.P. (2015). Atomically thin group V elemental films: theoretical investigations of antimonene allotropes. *ACS Applied Materials & Interfaces* 7: 11490–11496.

142 Nagao, T., Yaginuma, S., Saito, M. et al. (2005). Strong lateral growth and crystallization via two-dimensional allotropic transformation of semi-metal Bi film. *Surface Science* 590: 247–252.

143 Kumar, P., Singh, J., and Pandey, A.C. (2013). Rational low temperature synthesis and structural investigations of ultrathin bismuth nanosheets. *RSC Advances* 3: 2313–2317.

144 Aktürk, E., Aktürk, O.Ü., and Ciraci, S. (2016). Single and bilayer bismuthene: stability at high temperature and mechanical and electronic properties. *Physical Review B* 94: 014115.

145 Cheng, L., Liu, H., Tan, X. et al. (2014). Thermoelectric properties of a monolayer bismuth. *The Journal of Physical Chemistry C* 118: 904–910.

146 Boustani, I. (1997). New quasi-planar surfaces of bare boron. *Surface Science* 370: 355–363.

147 Feng, B., Zhang, J., Zhong, Q. et al. (2016). Experimental realization of two-dimensional boron sheets. *Nature Chemistry* 8: 563–568.

148 Mannix, A.J., Zhou, X.-F., Kiraly, B. et al. (2015). Synthesis of borophenes: anisotropic, two-dimensional boron polymorphs. *Science* 350: 1513.

149 Tai, G., Hu, T., Zhou, Y. et al. (2015). Synthesis of atomically thin boron films on copper foils. *Angewandte Chemie International Edition* 54: 15473–15477.

150 Zheng, B., Yu, H.-t., Lian, Y.-f., and Xie, Y. (2016). Novel α- and β-type boron sheets: theoretical insight into their structures, thermodynamic stability, and work functions. *Chemical Physics Letters* 648: 81–86.

151 Zhou, X.-F., Oganov, A.R., Wang, Z. et al. (2016). Two-dimensional magnetic boron. *Physical Review B* 93: 085406.

152 Li, J., Zhang, H., and Yang, G. (2015). Ultrahigh-capacity molecular hydrogen storage of a lithium-decorated boron monolayer. *The Journal of Physical Chemistry C* 119: 19681–19688.

153 Wu, C., Wang, H., Zhang, J. et al. (2016). Lithium–Boron (Li–B) monolayers: first-principles cluster expansion and possible two-dimensional superconductivity. *ACS Applied Materials & Interfaces* 8: 2526–2532.

154 Mir, S.H., Chakraborty, S., Jha, P.C. et al. (2016). Two-dimensional boron: lightest catalyst for hydrogen and oxygen evolution reaction. *Applied Physics Letters* 109: 053903.

155 Liu, L., Feng, Y.P., and Shen, Z.X. (2003). Structural and electronic properties of h-BN. *Physical Review B* 68: 104102.

156 Zhang, K., Feng, Y., Wang, F. et al. (2017). Two dimensional hexagonal boron nitride (2D-hBN): synthesis, properties and applications. *Journal of Materials Chemistry C* 5: 11992–12022.

157 Lee, J.S., Choi, S.H., Yun, S.J. et al. (2018). Wafer-scale single-crystal hexagonal boron nitride film via self-collimated grain formation. *Science* 362: 817–821.

158 Li, Q., Wu, Q., Gao, J. et al. (2018). Direct growth of 5 in. uniform hexagonal boron nitride on glass for high-performance deep-ultraviolet light-emitting diodes. *Advanced Materials Interfaces* 5: 1800662.

159 Pacile, D., Meyer, J.C., Girit, C.O., and Zettl, A. (2008). The two-dimensional phase of boron nitride: few-atomic-layer sheets and suspended membranes. *Applied Physics Letters* 92: 133107.

160 Dean, C.R., Young, A.F., Meric, I. et al. (2010). Boron nitride substrates for high-quality graphene electronics. *Nature Nanotechnology* 5: 722–726.

161 Cho, A.-J. and Kwon, J.-Y. (2019). Hexagonal boron nitride for surface passivation of two dimensional van der Waals heterojunction solar cells. *Acs Applied Materials & Interfaces* 11: 39765–39771.

162 Mendelson, N., Xu, Z.-Q., Toan Trong, T. et al. (2019). Engineering and tuning of quantum emitters in few-layer hexagonal boron nitride. *ACS Nano* 13: 3132–3140.

163 Ares, P., Cea, T., Holwill, M. et al. (2020). Piezoelectricity in monolayer hexagonal boron nitride. *Advanced Materials* 32.

164 Zhang, J., Tan, B., Zhang, X. et al. (2021). Atomically thin hexagonal boron nitride and its heterostructures. *Advanced Materials* 33.

165 Wang, X., Hossein, M., Wei, Z., and Xie, L. (2019). Growth of two-dimensional materials on hexagonal boron nitride (h-BN). *Nanotechnology* 30: 034003.

166 Splendiani, A., Sun, L., Zhang, Y. et al. (2010). Emerging photoluminescence in monolayer MoS_2. *Nano Lett* 10: 1271–1275.

167 Mak, K.F., Lee, C., Hone, J. et al. (2010). Atomically thin MoS_2: a new direct-gap semiconductor. *Phys Rev Lett* 105: 136805.

168 Kang, K., Lee, K.H., Han, Y. et al. (2017). Layer-by-layer assembly of two-dimensional materials into wafer-scale heterostructures. *Nature* 550: 229–233.

169 Chhowalla, M., Jena, D., and Zhang, H. (2016). Two-dimensional semiconductors for transistors. *Nature Reviews Materials* 1: 1–15.

170 Das, S., Chen, H.Y., Penumatcha, A.V., and Appenzeller, J. (2013). High performance multilayer MoS_2 transistors with scandium contacts. *Nano Lett* 13: 100–105.

171 Liu, Y., Huang, Y., and Duan, X. (2019). Van der Waals integration before and beyond two-dimensional materials. *Nature* 567: 323–333.

172 Lee, G.-H., Cui, X., Kim, Y.D. et al. (2015). Highly stable, dual-gated MoS_2 transistors encapsulated by hexagonal boron nitride with gate-controllable contact, resistance, and threshold voltage. *ACS Nano* 9: 7019–7026.

173 Dickinson, R.G. and Pauling, L. (1923). The crystal structure of molybdenite. *Journal of the American Chemical Society* 45: 1466–1471.

174 Feldman, Y., Wasserman, E., Srolovitz, D., and Tenne, R. (1995). High-rate, gas-phase growth of MoS_2 nested inorganic fullerenes and nanotubes. *Science* 267: 222–225.

175 Joensen, P., Frindt, R., and Morrison, S.R. (1986). Single-layer MoS_2. *Materials Research Bulletin* 21: 457–461.

176 Manzeli, S., Ovchinnikov, D., Pasquier, D. et al. (2017). 2D transition metal dichalcogenides. *Nature Reviews Materials* 2.

177 Freitas, D.C., Rodière, P., Osorio, M.R. et al. (2016). Strong enhancement of superconductivity at high pressures within the charge-density-wave states of 2*H*−TaS_2 and 2*H*−$TaSe_2$. *Physical Review B* 93: 184512.

178 Han, G.H., Duong, D.L., Keum, D.H. et al. (2018). Van der Waals metallic transition metal dichalcogenides. *Chem Rev* 118: 6297–6336.

179 Jiang, J., Liu, Z.K., Sun, Y. et al. (2017). Signature of type-II Weyl semimetal phase in $MoTe_2$. *Nat Commun* 8: 13973.

180 Choi, W., Choudhary, N., Han, G.H. et al. (2017). Recent development of two-dimensional transition metal dichalcogenides and their applications. *Materials Today* 20: 116–130.

181 Ali, M.N., Xiong, J., Flynn, S. et al. (2014). Large, non-saturating magnetoresistance in WTe_2. *Nature* 514: 205–208.

182 Keum, D.H., Cho, S., Kim, J.H. et al. (2015). Bandgap opening in few-layered monoclinic $MoTe_2$. *Nature Physics* 11: 482–486.

183 Arguello, C.J., Chockalingam, S.P., Rosenthal, E.P. et al. (2014). Visualizing the charge density wave transition in 2*H*–$NbSe_2$ in real space. *Physical Review B* 89.

184 Nagata, S., Aochi, T., Abe, T. et al. (1992). Superconductivity in the layered compound 2*H*–TaS_2. *Journal of Physics and Chemistry of Solids* 53: 1259–1263.

185 Pulkin, A. and Yazyev, O.V. (2016). Spin-and valley-polarized transport across line defects in monolayer MoS_2. *Physical Review B* 93: 041419.

186 Pi, L., Li, L., Liu, K. et al. (2019). Recent progress on 2D noble-transition-metal dichalcogenides. *Advanced Functional Materials* 29: 1904932.

187 Ataca, C., Şahin, H., and Ciraci, S. (2012). Stable, single-layer MX_2 transition-metal oxides and dichalcogenides in a honeycomb-like structure. *The Journal of Physical Chemistry C* 116: 8983–8999.

188 Pozo-Zamudio, O.D., Schwarz, S., Sich, M. et al. (2015). Photoluminescence of two-dimensional GaTe and GaSe films. *2D Materials* 2: 035010.

189 Davies, F.H., Price, C.J., Taylor, N.T. et al. (2021). Band alignment of transition metal dichalcogenide heterostructures. *Physical Review B* 103: 045417.

190 Silveri, F., Quesne, M.G., Roldan, A. et al. (2019). Hydrogen adsorption on transition metal carbides: a DFT study. *Phys Chem Chem Phys* 21: 5335–5343.

191 Zhang, H., Wang, Z., Zhang, Q. et al. (2019). Ti_3C_2 MXenes nanosheets catalyzed highly efficient electrogenerated chemiluminescence biosensor for the detection of exosomes. *Biosens Bioelectron* 124–125: 184–190.

192 Stottlemyer, A.L., Kelly, T.G., Meng, Q., and Chen, J.G. (2012). Reactions of oxygen-containing molecules on transition metal carbides: surface science insight into potential applications in catalysis and electrocatalysis. *Surface Science Reports* 67: 201–232.

193 Ahmad, S., Ashraf, I., Mansoor, M.A. et al. (2021). An overview of recent advances in the synthesis and applications of the transition metal carbide nanomaterials. *Nanomaterials (Basel)* 11: 776–810.

194 Huang, K., Li, Z., Lin, J. et al. (2018). Two-dimensional transition metal carbides and nitrides (MXenes) for biomedical applications. *Chem Soc Rev* 47: 5109–5124.

195 Anasori, B., Lukatskaya, M.R., and Gogotsi, Y. (2017). 2D metal carbides and nitrides (MXenes) for energy storage. *Nature Reviews Materials* 2: 16098.

196 Gogotsi, Y. and Anasori, B. (2019). The rise of MXenes. *ACS Nano* 13: 8491–8494.

197 Jiang, Q., Lei, Y., Liang, H. et al. (2020). Review of MXene electrochemical microsupercapacitors. *Energy Storage Materials* 27: 78–95.

198 Alhabeb, M., Maleski, K., Anasori, B. et al. (2017). Guidelines for synthesis and processing of two-dimensional titanium carbide ($Ti_3C_2T_x$ MXene). *Chemistry of Materials* 29: 7633–7644.

199 Yang, J., Naguib, M., Ghidiu, M. et al. (2016). Two-dimensional Nb-based M_4C_3 solid solutions (MXenes). *Journal of the American Ceramic Society* 99: 660–666.

200 Chen, C., Xie, X., Anasori, B. et al. (2018). MoS_2 -on-MXene heterostructures as highly reversible anode materials for lithium-ion batteries. *Angew Chem Int Ed Engl* 57: 1846–1850.

201 Xu, B. and Gogotsi, Y. (2020). MXenes: from discovery to applications. *Advanced Functional Materials* 30: 2007011.

202 Weinberger, C.R. and Thompson, G.B. (2018). Review of phase stability in the group IVB and VB transition-metal carbides. *Journal of the American Ceramic Society* 101: 4401–4424.
203 Gusev, A.I. (2000). Order–disorder transformations and phase equilibria in strongly nonstoichiometric compounds. *Physics-Uspekhi* 43: 1–37.
204 Hwang, H.Y., Iwasa, Y., Kawasaki, M. et al. (2012). Emergent phenomena at oxide interfaces. *Nature Materials* 11: 103–113.
205 Osada, M. and Sasaki, T. (2009). Exfoliated oxide nanosheets: new solution to nanoelectronics. *Journal of Materials Chemistry* 19: 2503–2511.
206 Kalantar-zadeh, K., Ou, J.Z., Daeneke, T. et al. (2016). Two dimensional and layered transition metal oxides. *Applied Materials Today* 5: 73–89.
207 Mannhart, J. and Schlom, D.G. (2010). Oxide interfaces-an opportunity for electronics. *Science* 327: 1607–1611.
208 Chimene, D., Alge, D.L., and Gaharwar, A.K. (2015). Two-dimensional nanomaterials for biomedical applications: emerging trends and future prospects. *Advanced Materials* 27: 7261–7284.
209 Surnev, S., Ramsey, M.G., and Netzer, F.P. (2003). Vanadium oxide surface studies. *Progress in Surface Science* 73: 117–165.
210 Walia, S., Balendhran, S., Nili, H. et al. (2013). Transition metal oxides – thermoelectric properties. *Progress in Materials Science* 58: 1443–1489.
211 Ganduglia-Pirovano, M.V., Hofmann, A., and Sauer, J. (2007). Oxygen vacancies in transition metal and rare earth oxides: current state of understanding and remaining challenges. *Surface Science Reports* 62: 219–270.
212 Carrasco, J., Lopez, N., Illas, F., and Freund, H.J. (2006). Bulk and surface oxygen vacancy formation and diffusion in single crystals, ultrathin films, and metal grown oxide structures. *Journal of Chemical Physics* 125: 074711.
213 Tan, C., Cao, X., Wu, X.-J. et al. (2017). Recent advances in ultrathin two-dimensional nanomaterials. *Chemical Reviews* 117: 6225–6331.
214 Balendhran, S., Walia, S., Nili, H. et al. (2013). Two-dimensional molybdenum trioxide and dichalcogenides. *Advanced Functional Materials* 23: 3952–3970.
215 Sun, Y., Sun, Z., Gao, S. et al. (2012). Fabrication of flexible and freestanding zinc chalcogenide single layers. *Nature Communications* 3: 1057.
216 Enjalbert, R., Lecante, P., and Galy, J. (1986). A refinement of the structure of V_2O_5. *Acta Crystallographica Section C: Crystal Structure Communications* 42: 1467–1469.
217 Dou, Y., Zhang, L., Xu, X. et al. (2017). Atomically thin non-layered nanomaterials for energy storage and conversion. *Chemical Society Reviews* 46: 7338–7373.
218 Tan, C. and Zhang, H. (2015). Wet-chemical synthesis and applications of non-layer structured two-dimensional nanomaterials. *Nature Communications* 6: 7873.
219 Sun, Y., Gao, S., and Xie, Y. (2014). Atomically-thick two-dimensional crystals: electronic structure regulation and energy device construction. *Chemical Society Reviews* 43: 530–546.

220 Zhou, N., Yang, R., and Zhai, T. (2019). Two-dimensional non-layered materials. *Materials Today Nano* 8: 100051.

221 Bauer, E. and van der Merwe, J.H. (1986). Structure and growth of crystalline superlattices: from monolayer to superlattice. *Physical Review. B, Condensed Matter* 33: 3657–3671.

222 Thiel, S., Hammerl, G., Schmehl, A. et al. (2006). Tunable quasi-two-dimensional electron gases in oxide heterostructures. *Science* 313: 1942–1945.

223 Sahoo, T., Nayak, S.K., Chelliah, P. et al. (2016). Observations of two-dimensional monolayer zinc oxide. *Materials Research Bulletin* 75: 134–138.

224 Liu, K.-K., Zhang, W., Lee, Y.-H. et al. (2012). Growth of large-area and highly crystalline MoS_2 thin layers on insulating substrates. *Nano Letters* 12: 1538–1544.